Gold Nanoparticle-Enhanced and Size-Dependent Generation of Reactive Oxygen Species from Protoporphyrin IX

Maung Kyaw Khaing Oo,[†,⊥] Yamin Yang,[‡] Yue Hu,[†] Maria Gomez,[§] Henry Du,[†,*] and Hongjun Wang[‡,*]

[†]Department of Chemical Engineering and Materials Science and [‡]Department of Chemistry, Chemical Biology and Biomedical Engineering, Stevens Institute of Technology, Hoboken, New Jersey 07030, United States, and [§]Department of Chemistry and Biochemistry, Drew University, Madison, New Jersey 07940, United States. [⊥]Present address: Department of Biomedical Engineering, University of Michigan, Ann Arbor, MI 48109.

ABSTRACT Photosensitizer, protoporphyrin IX (PpIX), was conjugated with Au nanoparticles (Au NPs) of 19, 66, and 106 nm diameter to study the size-dependent enhancement of reactive oxygen species (ROS) formation enabled by Au NPs. The ROS enhancement ratio is determined to be 1:2.56:4.72 in order of increasing Au NP size, in general agreement with theoretically calculated field enhancement to the fourth power. The convergence of the experimental and simulated results suggests that Au NP-enhanced and size-dependent ROS formation can be attributed directly to the localized electromagnetic field as a result of surface plasmonic resonance of Au NPs under light irradiation. *In vitro* study on the ROS formation enabled by PpIX-conjugated Au NPs in human breast cancer cells (MDA-MB-231) revealed the similar size-dependent enhancement of intracellular ROS formation, while the enhancement greatly depended on cellular uptake of Au NPs. Cellular photodynamic therapy revealed that cell destruction significantly increased in the presence of Au NPs. Compared to the untreated control (0% destruction), 22.6% cell destruction was seen in the PpIX alone group and more than 50% cell destruction was obtained for all PpIX-conjugated Au NPs. The 66 nm Au NPs yielded the highest cell destruction, consistent with the highest cellular uptake and highest ROS formation. Clearly, the complex cellular environment, size-dependent cellular uptake of Au NPs, and ROS generations are vital contributors to the overall cellular PDT efficacy.

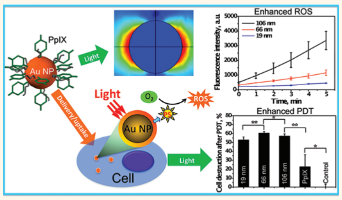

KEYWORDS: gold nanoparticles · reactive oxygen species · protoporphyrin IX · photodynamic therapy · surface plasmon resonance · surface-enhanced Raman scattering

Reactive oxygen species (ROS) are oxidative radicals (*e.g.*, HO•, O_2^-, H_2O_2) formed upon incomplete reduction of oxygen.[1] In addition to their well-known role in redox signaling,[2] ROS can cause oxidation of DNA, amino acid, and lipid, potentially leading to the development of various diseases and cell apoptosis and necrosis.[3] On the other hand, the oxidative nature of ROS can be used as a therapeutic means to eradicate diseased cells, which forms the basis for cancer treatment using photodynamic therapy (PDT). PDT, a minimally invasive technique for cancer therapy, involves the administration of a photosensitizing compound (also called photosensitizer, PS) and subsequent light irradiation at an appropriate wavelength to induce ROS for selectively damaging cancerous cells and tissues.[4,5] Formation of elevated ROS is clearly the key for effective PDT of cancers.

Numerous PSs have been developed to generate ROS. Characteristics of an ideal PS have been well-documented.[6,7] Low administration toxicities,[8] reliable photoactivation, and controllable selectivity/targetability are among the selection criteria for clinically relevant PS. Current clinical PSs mainly originate from porphyrins, chlorophylls, and dyes.[7] Porphyrin families have a long evolution history[9−11] and are extensively adopted for clinical applications; for example, Photofrin has been approved by FDA for its use in treating early and late endobronchial lesions as well as Barrett's esophagus and esophageal obstructing lesions.[12] In addition, 5-aminolevulinic acid (5-ALA), an enzymatically convertible precursor of PpIX,[13] has shown a high success against the skin basal cell and squamous cell cancers[14,15] apart from its FDA-approved use for outpatient treatment of actinic keratosis.

With appealing clinical evidence of the effectiveness of PDT, its application somehow is mainly confined to the superficial treatment due to the limited PS and light penetration in the tissue. In the search for a more effective route to deliver PS to deep tissue and targeted cells, nanoparticles are often used as a carrier considering their high specific surface area for further modification

* Address correspondence to
hdu@stevens.edu,
hongjun.wang@stevens.edu.

Received for review April 24, 2011
and accepted March 2, 2012.

10.1021/nn300327c

to render the hydrophilicity and improve cellular uptake. This becomes even more relevant to those hydrophobic PSs that are difficult to administer for *in vivo* applications.[16] For this purpose, the nanoparticles can be biodegradable polymer-based, such as chitosan[17] and poly(lactic acid),[18] or inorganic material-based, such as silica,[19] quantum dots,[20] and gold.[21] With the aid of nanoparticles, selective accumulation of PS in tumorous tissue can be achieved for targeted therapy[22] and for the simultaneous detection of ROS-induced cell response.[23] The latest pioneering progresses based on the chemical nature of nanoparticles were described in a recent review paper.[24] Besides drug carrier functionality, metallic nanoparticles have an additional unique property (*i.e.*, localized plasmonic field), which can enhance electric field near the nanostructure. Among various metallic nanoparticles, Au nanoparticles (Au NPs) have been broadly explored for drug delivery and photothermal therapy due to their biocompatibility,[25] chemical stability,[26] and strong light absorption at tunable plasmon resonance wavelength.[27−29] The functionalization of the Au NP surface with PS can be achieved *via* strong covalent bonding or weak interactions such as van der Waals interactions and electrostatic interactions.[24] We have shown recently in an *in vitro* study that electrostatically conjugated 5-ALA-Au NP could significantly enhance the PDT of cancer cells.[30] A possible explanation for this exciting observation can be ascribed to the enhanced generation of ROS from PS as a result of the highly localized plasmonic field of the Au NPs and their aggregates. It has been well-established that the plasmonic field of metal nanoparticles is closely regulated by the particle size.[31] We therefore further postulate that the enhanced generation of ROS may also be correlated with the size of Au NPs. Confirmation of this hypothesis can better guide our efforts in developing effective strategies for Au NP-assisted PDT with the potential to increase the treatment depth while reducing light dose and PS concentration.

To ascertain the contribution of plasmonic effect to ROS formation as well as determine the size-dependent ROS enhancement, protoporphyrin IX (PpIX) as a model PS and positively charged Au NPs of three different sizes were used. Positively charged Au NPs could facilitate the binding of PpIX with Au NPs *via* electrostatic interaction. In this regard, Au NPs acted as both an ROS enhancer and a PS drug carrier. Three representative particle sizes (19, 66, and 106 nm in diameter) were synthesized and used. Au NP-assisted ROS formation was first investigated with cell-free conditions, in which ROS formation increased with Au NP size. To better elucidate the size dependence, we performed theoretical simulation of the electromagnetic field enhancement by Au NPs using RF Module 3.5a of COMSOL Multiphysics software. Surface-enhanced Raman scattering measurement of a marker molecule with various sizes of Au NPs further confirmed the size dependence of the Au NP-enhanced plasmonic field. Clearly, the simulation result correlated well with the experimental measurements. In contrast to the well-controlled cell-free conditions, the complexity of the biological system could drastically interfere with such an observation. To this end, we further investigated whether such size-dependent ROS formation could similarly occur inside the cell. Human breast cancer cells were treated with electrostatically conjugated PpIX–Au NPs of different sizes to investigate their effect on PDT treatment. The cellular uptake of various Au NPs was size-dependent, with 66 nm Au NPs yielding the highest uptake. Following the same trend, 66 nm Au NPs displayed the highest enhancement of singlet oxygen species formation, which in turn led to the lowest viability of cancer cells after PDT treatment. However, the size dependence in a cellular environment is not as strong as under cell-free conditions, suggesting possible involvement of an intracellular self-defensive mechanism against oxidative stress.

TABLE 1. Characteristics of Three Different Sizes of Au NPs

Au NPs	1#	2#	3#
BPEI (mg/mL)	2	1.4	1.2
$HAuCl_4$ (mM)	4	4	4
average size (nm)	19 ± 5	66 ± 10	106 ± 12
maximum absorbance wavelength (nm)	520	527	531
zeta-potential (mV)	47.8 ± 33.3	60.1 ± 16.2	70.2 ± 16.5

RESULTS AND DISCUSSION

There are different approaches to make Au NPs. Literature work has mostly followed the conventional citrate-reducing method[32,33] to produce Au NPs that are inherently negatively charged. In this study, we used branched polyethyleneimine (BPEI) (molecular weight 10 000) as the reducing agent for $HAuCl_4$ in order to obtain positively charged Au NPs (see details in the Experimental Section and Table 1). Monodisperse Au NPs with three distinct size disparities of 19 ± 5, 66 ± 10, and 106 ± 12 nm were prepared by adjusting the respective BPEI concentrations of 2, 1.4, and 1.2 mg/mL while maintaining a constant $HAuCl_4$ concentration of 4 mM in an aqueous solution. Shown in Figure 1a−c are SEM micrographs of the resultant Au NPs. The average Au NP sizes were determined based on high-resolution SEM images from at least five randomly selected locations, and their corresponding size distributions were exhibited in Figure 1d−e. The relatively narrow size distribution can prevent the unwanted overlap between the adjacent Au NP groups, allowing for a definitive correlation between Au NP size and ROS enhancement. UV−visible absorption spectra of various Au NP colloids are shown in Figure 1g, with the maximum absorbance wavelength,

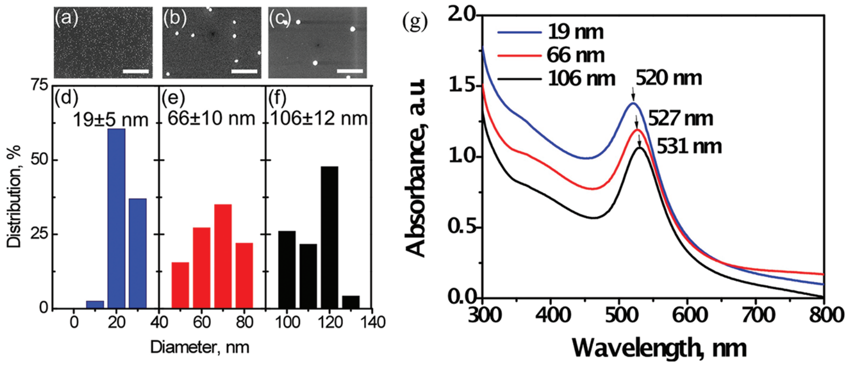

Figure 1. SEM micrographs of Au NPs of (a) 19 nm, (b) 66 nm, and (c) 106 nm in diameter. The scale bar represents 1 μm. Size distribution histograms of three different Au NPs, (d) 19 nm, (e) 66 nm, and (f) 106 nm, and (g) their corresponding UV–vis absorption spectra.

or surface plasmon resonance wavelength, gradually shifted from 520 nm for the smallest Au NPs (*i.e.*, 19 nm) to 531 nm for the largest ones (*i.e.*, 106 nm). The red shift with increasing particle size can be attributed to the phase retardation, an electrodynamic phenomenon.[34] The zeta-potentials of Au NPs were measured, and they all remained positively charged after being washed with deionized water (Table 1), indicating a strong interaction between BPEI and Au NPs.

Adding PpIX to the positively charged Au NP colloidal solution under a dark condition would lead to the formation of PpIX–Au NP conjugates *via* electrostatic interaction between the negatively charged carboxylate (–COO–) groups of PpIX[35] and positively charged amine (NH– and NH_2–) groups of BPEI (Figure 2a). The proximity of PpIX to the Au NP surface is necessary for efficient energy transfer from Au NPs to PpIX. Light irradiation at 532 nm could promote PpIX to an excited state. Energy released due to de-excitation of PpIX would be subsequently transferred to neighboring oxygen to form ROS (Figure 2b).[8] The resultant ROS can be monitored at its emission wavelength of 1270 nm as reported by Samia *et al.*[36] However, the short lifetime of ROS, typically in the order of nanoseconds, makes direct measurement of ROS extremely challenging. Nevertheless, various ROS probes are available for indirect measurement.[37] In this study, in order to detect the ROS formation, we used a nonfluorescent dihydrorhodamine 123 (DHR123) as a universal ROS tracking agent,[38] which was converted to fluorescent Rhodamine 123 (R123) upon reaction with ROS (Figure 2c) (see details in Experimental Section).

Neither Au NPs nor PpIX was fluorescent at the wavelength of 528 nm, but DHR123 had detectable fluorescence after irradiation and the fluorescence intensity slowly increased with irradiation time (see Figure S1 in the Supporting Information). The irradiation-induced fluorescence increase is a result of the slow oxidation of DHR123 by ambient oxygen, indicating its sensitivity to ROS measurement.[38] With respect to the sensitivity of DHR123 to irradiation, it became necessary to determine whether the presence of Au NPs would also affect the conversion of DHR123 into R123 without the presence of photosensitizer, PpIX. A slight increase of fluorescence intensity was similarly observed under irradiation especially with larger Au NPs (66 and 106 nm); however, the increase was slow and not significant (see Supporting Information Figure S1) and its contribution to the measurement of PpIX–Au NP-induced ROS formation could be eliminated by subtracting the corresponding background values.

Depicted in Figure 3 is time-resolved alteration of R123 fluorescence intensity in the presence of PpIX–Au NP conjugates. There, the conversion of R123 from DHR123 was proportional to ROS concentration. Clearly, the fluorescent intensity was strongly correlated to the size of Au NPs. On the basis of the fluorescent measurement, the enhancement ratio was 1:3.33:11.65 for 19, 66, and 106 nm Au NPs, respectively. This measured enhancement comprised two possible contributions: surface-enhanced fluorescence of the end product of R123 by Au NPs and enhanced conversion of DHR123 to R123 as a result of elevated ROS generation by Au NPs. By directly measuring the fluorescence intensity of R123–Au NP solution mixtures of 19, 66, and 106 nm in particle sizes, the corresponding fluorescence enhancement ratio was 1:1.3:2.47 (see Supporting Information Figure S2). Offsetting the R123 contribution from the original set of fluorescent enhancement ratio of the PpIX–Au NP conjugates, we calculated the ROS part of the enhancement ratio involving 19, 66, and 106 nm Au NPs to be 1:2.56:4.72. Our experimental results clearly suggest a strong correlation between ROS generation and the size of Au NPs.

To better elucidate the size dependence of ROS formation by Au NPs, we performed theoretical simulation of the electromagnetic field enhancement by Au NPs with particle size as a parameter using the RF Module 3.5a of COMSOL Multiphysics software package. By utilizing the values of complex dielectric function of Au at different wavelengths reported by Johnson and Christy,[39]

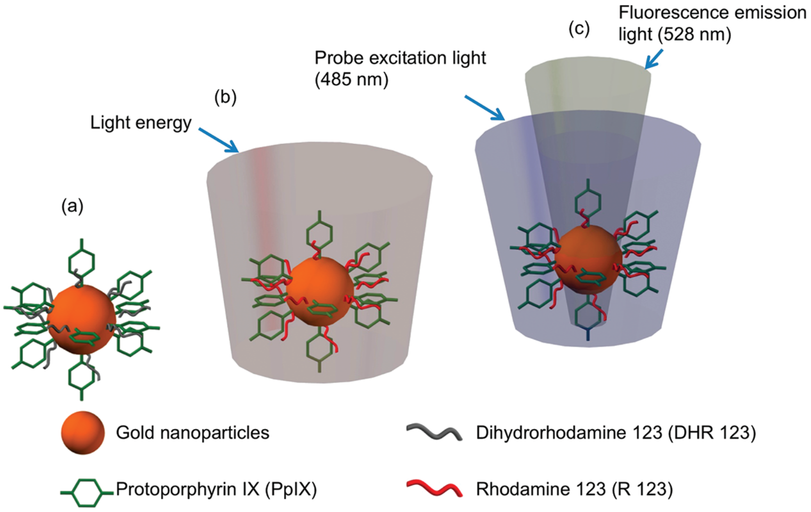

Figure 2. Schematic illustration of ROS enhancement by Au NPs. (a) PpIX and Au NP conjugation, (b) light irradiation (532 nm, 24 mW), and (c) fluorescence measurement at 528 nm *via* 485 nm excitation.

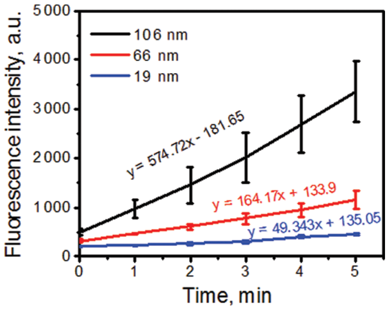

Figure 3. Kinetics of ROS formation of PpIX-conjugated Au NPs with tracking agent DHR123.

widely adopted by the modeling community, and applying the Mie scattering theory,[27] we calculated the particle size-dependent electric field scattering in the wavelength range of 450 and 600 nm. The corresponding results are shown in Figure 4. The field intensity has a weak dependence on excitation wavelength below 480 nm (Figure 4a). Above this wavelength, however, the field increases significantly with both the size of Au NPs and the wavelength. The respective simulation images of electromagnetic field distribution for 20, 60, and 100 nm Au NPs at 530 nm excitation wavelength are depicted in Figure 4b–d. At this wavelength, the calculated maximum electric field ratio for 20, 60, and 100 nm Au NPs is 1:1.18:1.34, in agreement with previous calculations.[27] We note that in surface-enhanced Raman scattering (SERS), a phenomenon attributed strongly to localized plasmonic field, the SERS enhancement is proportional to the fourth power of the electric filed ($|E|^4$).[40−42] The fourth power of our calculated field ratio is 1:1.94:3.22, in qualitative agreement with that of the experimentally determined size-dependent ROS enhancement of 1:2.56:4.72. The stronger dependence shown in the experiments may be a result of the clustering of Au NPs, which is known to lead to the formation of electromagnetic "hot spots". As such, our simulation based on discrete nanoparticles represents only the lower bound of the anticipated field enhancement. Nevertheless, the general consistency of the theoretical predication and experimental results further confirm that ROS generation is significantly enhanced by localized plasmonic field of Au NPs. The larger the particles are, the stronger the effect is.

In light of the fact that the localized plasmonic field of Au NPs plays a similar role in both ROS and SERS enhancement, we also carried out SERS experiments with Au NPs of all three sizes immobilized on silicon substrates using R123 aqueous solution as a model analyte to establish the general experimental consistency of our findings. Shown in Figure 5 are the SERS spectra obtained from 10^{-9} M R123 with particle size as a parameter. Raman background spectrum from 106 nm Au NPs is included for reference. Clearly, the 106 nm Au NP is most SERS-active, resulting in strong and distinct Raman spectral features. The bands at 1555 cm^{-1} (xanthene ring stretching), 1611 cm^{-1} (external phenyl ring stretching), and 1642 cm^{-1} (xanthene ring stretching) are characteristic of R123.[43] On the other hand, both 19 and 66 nm Au NPs could not yield detectable spectral features for R123 at 10^{-9} M, indicating their weaker SERS enhancement compared to 106 nm Au NPs. The size-dependent SERS enhancement phenomenon is similarly observed in a recent report on the detection of 2,4-dinitrotoluene (DNT) vapor using glass-slide-immobilized Au NPs.[44] Clearly, the experimental results on size dependence of Au NP-induced ROS generation and SERS enhancement are self-consistent and agree with the theoretical prediction. However, these results were based on a well-controlled cell-free experimental setup, and it would be of great significance to study the size dependence of Au NP-enhanced ROS formation in a biological setting, relevant to clinical application for PDT treatment of cancer. In this

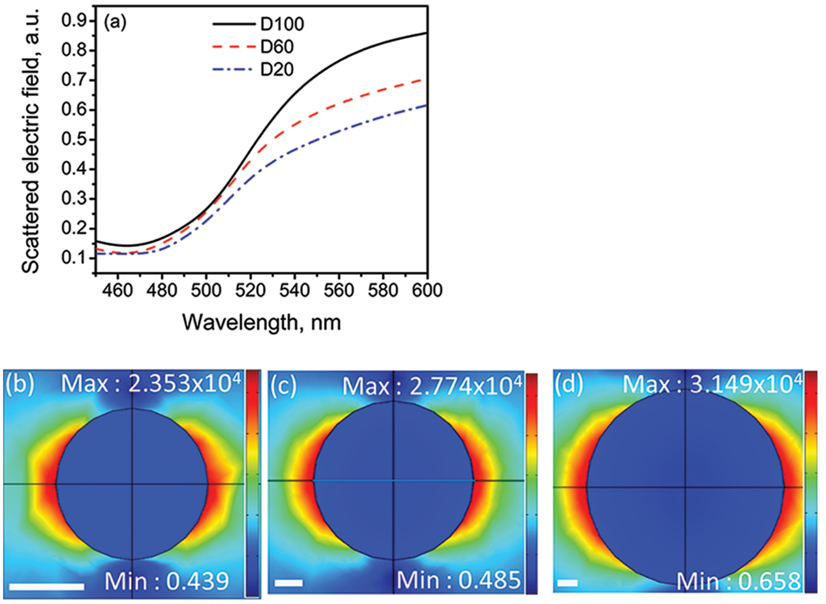

Figure 4. (a) Simulated field scattering maximum of Au NP of three particle sizes in the excitation wavelength range of 450 and 600 nm, and electric field distribution at 530 nm excitation for (b) 20 nm, (c) 60 nm, and (d) 100 nm Au NPs. The scale bar is 10 nm.

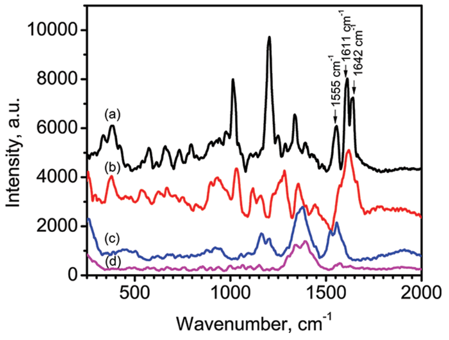

Figure 5. Raman spectra of 10^{-9} M R123 aqueous solution obtained using (a) 106 nm, (b) 66 nm, and (c) 19 nm Au NPs immobilized on silicon substrates. (d) Background Raman spectrum of 106 nm Au NPs. The spectra were acquired using 785 nm excitation wavelength at 100 mW. Acquisition time was 20 s.

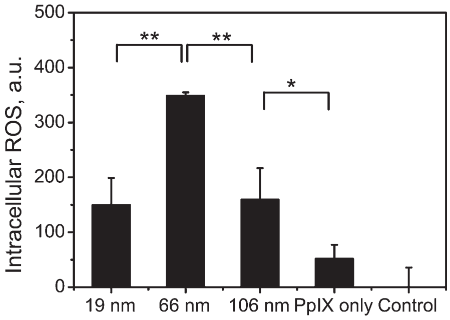

Figure 6. Elevated generation of singlet oxygen in MDA-MB-231 human breast cancer cells after various PDT treatments with PpIX-conjugated 19, 66, and 106 nm Au NPs, PpIX only, and controls (without PpIX and Au NPs) and light irradiation for 1 min. The singlet oxygen was measured using singlet oxygen sensor green reagent (SOSG, Sigma). The data are representative of three separate experiments; $^{**}p < 0.005$, $^{*}p < 0.05$.

regard, Au NPs of all three sizes were further evaluated for their contribution to cellular ROS formation and the corresponding PDT efficacy with PpIX as the exogenous photosensitizer.

The compatibility of various Au NPs to human breast cancer cells (MDA-MB-231) was first evaluated by supplementing Au NPs into the culture and incubating for 24 h at 37 °C. The cell viability was determined by the thiazolyl blue tetrazolium bromide (MTT, Sigma) assay. The result showed that there was no difference in cell viability among Au NP-treated groups (all three sizes) and the untreated controls (data not shown), suggesting the superior biocompatibility of Au NPs, which is consistent with previous reports.[30] In order to evaluate the size-dependent intracellular ROS formation enabled by Au NPs, human breast cancer cells were incubated with various PpIX-conjugated Au NPs at a fixed concentration, irradiated, and then quantified for intracellular singlet oxygen species with the singlet oxygen sensor green reagent (SOSG) (see Experimental Section). The results showed that elevated ROS levels were measured for all of the groups treated with PpIX-conjugated with or without Au NPs, and meanwhile, a relatively high level of endogenous oxidative stress was indeed detected in the untreated control group, similar to the findings reported elsewhere.[45] In general, various redox systems such as the glutathione and NADH couples inside the cells could effectively balance the cellular oxidative stress and maintain it at a rather low level.[46] However, the well-balanced mechanism is interrupted in cancer cells due to the constitutively activated mitogenic pathways and transformed metabolic pathways, resulting in a

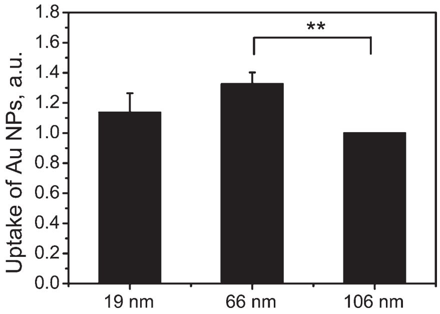

Figure 7. Uptake of different size of Au NPs (19, 66, and 106 nm) after incubation for 4 h with human breast cancer cells (MDA-MB-231). The uptakes were quantified by spectrometric assay. The data presented are the average of three separate experiments; **$p < 0.005$.

high cumulative endogenous ROS level.[47] To determine the intracellular ROS formation directly coming from exogenous PpIX and Au NP enhancement, the endogenous ROS contribution was excluded from the measurement and the result is summarized in Figure 6. Consequently, the ROS enhancement ratio for PpIX-conjugated Au NPs was determined to be 2.90 ± 0.95 (19 nm):6.75 ± 0.12 (66 nm):3.08 ± 1.11 (106 nm), respectively, compared to PpIX only. The 66 nm Au NPs yielded the highest ROS enhancement, and the ratio between 19 and 66 nm Au NPs is 1:2.3, close to the cell-free measurement (1:2.56). To our surprise, the intracellular ROS enhancement by 106 nm Au NPs, somehow, was similar to that of 19 nm Au NPs, much lower than the enhancement ratio from the cell-free studies (Figure 3). Obviously, the enhancement of intracellular ROS formation greatly relies on the availability of Au NPs inside the cells. Although the same amount of Au NPs for all of the sizes was initially added to the culture, the particle size might significantly regulate the cellular uptake of Au NPs based on the observation from a previous report on the negatively charged Au NPs in mammalian cells.[48] Indeed, our measurement clearly showed that the intracellular uptake of positively charged Au NPs also depended on the particle size (Figure 7). After incubation for 4 h, 106 nm Au NPs exhibited the lowest uptake among all three sizes and 66 nm gave the highest uptake though the difference between 19 and 66 nm was not statistically significant. Most likely, it is the limited availability of 106 nm Au NPs inside the breast cancer cells that accounts for the low intracellular ROS enhancement. In the meanwhile, after endocytosis by the cells, large Au NPs could be trapped in the vesicles in the cytoplasm with limited access to PpIX. The shape and size of the aggregated particles may vary, and the neighboring protein molecules could make the situation even more complicated.

It is known that cancer cell destruction in PDT treatment is closely correlated with the intracellular ROS level.[12] With the increase of intracellular ROS level by Au NPs, higher cell destruction is expected. To confirm this and determine whether cell destruction

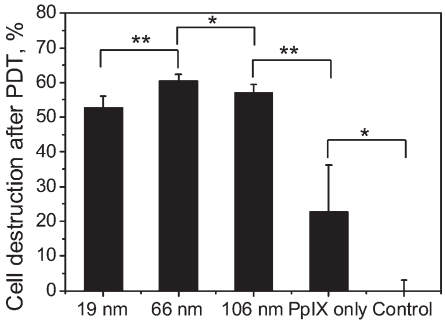

Figure 8. Destruction of human breast cancer cells (MDA-MB-231) determined by MTT assay after various PDT treatments where cells were incubated with PpIX-conjugated 19, 66, and 106 nm Au NPs, PpIX only, and the sham control without PpIX and Au NPs for 4 h, and then irradiated for 1 min under a 150 W halogen light. The cells were subsequently cultured for 24 h prior to MTT measurement. The data presented are the average of three separate experiments; *$p < 0.05$, **$p < 0.005$.

by PDT treatment was also dependent on Au NP size, the culture after 24 h was analyzed for cell viability by measuring the metabolic activity *via* MTT assay. Compared to the untreated control (0% destruction), 22.6% cell destruction was seen in the PpIX alone group and more than 50% cell destruction was obtained for all the PpIX-conjugated Au NPs (Figure 8). Although the 66 nm Au NP–PpIX yielded the highest destruction of breast cancer cells (60.4%), the cell destruction ratio between 19 and 66 nm Au NPs was only 1:1.15 and did not fully comply with the ROS enhancement ratio. Distinct from the straightforward ROS formation enhanced by PpIX–Au NPs, the ROS-triggered cell killing comprises the apoptosis or in combination with necrosis mechanism, depending on the location of ROS formation and ROS dosage. Either cell killing mechanism involves multiple signaling pathways, for example, various caspase isoforms in the apoptosis and the Toll-like receptors in necrosis.[49,50] Further complicated by the anti-apoptotic and pro-apoptotic regulation of Bcl-2 family in mitochondria, the size-dependent PpIX–Au NP-induced cell destruction *via* ROS becomes less proportional to the ROS enhancement. In this regard, our future studies will further understand the localized intracellular ROS formation enabled by Au NPs and correlate the cell destruction with ROS formation, which can allow us to better design the Au NP-enabled PDT treatment. Taken together, our results confirmed that the presence of Au NPs in PpIX-PDT treatment could significantly enhance the cell destruction efficacy and the enhanced PDT efficacy partially depended on the particle size.

CONCLUSION

We have demonstrated that ROS formation by light irradiation of PpIX photosensitizer is significantly enhanced by Au NPs. The convergence of experimental findings and theoretical simulation on the size dependence of the enhancement and the electrical field intensity, respectively, suggests that the enhanced ROS generation in the presence of Au NPs can be attributed to the contribution of the high localized plasmonic field, which increases with particle size in the range of study. Moreover, the Au NP-enhanced PDT efficacy in MDA-MB-231 human breast cancer cells indicates the importance of Au NP size-dependent intracellular uptake and complex cellular environment. We postulate that the phenomenon of Au NP-enhanced ROS formation can be similarly found with the use of other photosensitizers and thus will have general applicability to PDT. The observed size dependence will be a significant guide toward further study of Au NP-assisted PDT.

EXPERIMENTAL SECTION

Materials. Gold(III) chloride solution (30 wt % of $HAuCl_4$ in dilute HCl), branched polyethyleneimine (BPEI) (molecular weight 10 000), protoporphyrin IX (PpIX), and dihydrorhodamine-123 (DHR123) were purchased from Sigma-Aldrich (St. Louis, MO, USA). They were used without further purification. Milli-Q water was filtered by Quantum Ex, Ultrapure Oranex Cartridge filtration columns (Millipore, Billerica, MA, USA) and used for all experiments.

All glassware and silicon wafers were cleaned overnight in the mixture solution prepared by dissolving 120 g of Nochromix powder (Godax Laboratories, Inc., MD, USA) in 3.78 L of concentrated sulfuric acid and then thoroughly rinsed with Milli-Q water. Fetal bovine serum (FBS) was purchased from American Type Culture Collection (ATCC, Manassas, VA, USA). All other cell culture reagents and solutions were obtained from Invitrogen (Carlsbad, CA, USA) except as indicated.

Synthesis of Gold Nanoparticles. $HAuCl_4$ and branched polyethyleneimine (BPEI) (molecular weight = 10 000) were mixed at various concentrations. The solution mixture was stirred for 5 min in an ice bath and subsequently placed under a metal halide UV lamp (400 W, Cure Zone 2) for 1 h. Upon completion of the reduction reaction, the color of the solution mixture changed from yellow to dark red. Specifically, equal volumes of 4 mM of $HAuCl_4$ and BPEI concentration of 2, 1.4, and 1.2 mg/mL were mixed to produce positively charged gold nanoparticles (Au NPs) of ~19, ~66, and ~106 nm in diameter, respectively.

Characterization of Gold Nanoparticles. The sizes of Au NPs were examined by a LEO 982 FEG scanning electron microscope (SEM) (Carl Zeiss SMT Inc., Peabody, MA, USA) in conjunction with ImageJ analysis software. The average coverage and standard deviation data were obtained from high-resolution SEM images of five different locations on each sample. Au NPs wers further diluted 5−7 times in deionized water for ζ-potential measurement using a Zetasizer Nano Z (Malvern Instruments Ltd., Worcestershire, UK).

Kinetics of ROS Formation. Au NP colloidal solutions (50 μL) of various particle sizes were mixed with 50 μL of 10 μM protoporphyrin IX (PpIX) photosensitizer to study the effect of Au NPs on ROS formation. Dihydrorhodamine-123 (DHR123, nonfluorescent) was used as a universal ROS tracking agent.[38] Oxidation of DHR123 by ROS resulted in formation of fluorescent Rhodamine 123 (R123). Then, 50 μL of 10 μM DHR123 was subsequently added to the mixture under dark condition. Final concentrations of 0.67 mM Au NPs, 3.33 μM DHR123, and 3.33 μM PpIX concentrations were maintained constant for all measurements. Total volume of 150 μL samples ($n = 3$) in 96-well plates was irradiated by 24 mW of 532 nm coherent laser light for different time durations. The fluorescence measurements were done after 1 min irradiation using a multimode microplate reader (Synergy HT, BioTek Instruments, Inc., Winooski, VT, USA) at an excitation wavelength of 485/20 nm and an emission wavelength of 528/20 nm.

Surface-Enhanced Raman Measurement. Au NPs of the three sizes were deposited on the silicon wafer to achieve SERS-active substrates for measurements of 1×10^{-9} M Rhodamine 123. Raman measurements were carried out with an in-house built Raman imaging and spectroscopy system. The system involved 785 nm laser excitation, 300 groove/mm grating spectrometer (Acton series spectrograph SP2300, focal length 300 mm) attached with spectroscopy grade CCD (Princeton instruments, SPEC-10), and high sensitivity imaging grade CCD (Princeton Instruments, PIXIS 1024 BR). Raman images and spectra were synchronized during acquisition. The same 100× Nikon CFI60 microscope objective was used for laser excitation as well as collection of the Raman signal.

Simulation. A Dell OptiPlex desktop was used to perform high mesh density simulation of nanoparticles. The specification of the computer was Intel(R) Core(TM)2 Quad CPU Q9650 at 3.00 GHz with 8GB RAM. The operating platform was 64-bit Windows 7 professional. For the simulation of plasmonic properties of gold nanoparticles, RF module, an extended version of COMSOL Multiphysics 3.5a version, was used. The desired particle size and shape in 3D were drawn in draw mode using the Cartesian coordinate system. Boundary conditions and perfectly matched layer (PML) were also defined in the draw mode. Simulation duration for a single nanoparticle took about 4−8 h.

Cell Seeding and Culture. Human breast cancer cells (MDA-MB-231, ATCC) were cultured in L-15 medium (Leibovitz) (Sigma) supplemented with 10% fetal bovine serum and 1% penicillin/streptomycin in a humidified incubator at 37 °C without CO_2. For PDT experiment, cells were seeded into a 96-well plate at the concentration of 1.5×10^4 cells/mL and then cultured for 48 h prior to treatment.

Cellular Photodynamic therapy (cPDT). The PDT procedure was conducted according to our previous study.[30] Briefly, the medium of cell-seeded well plates was replaced with the serum-free medium containing PpIX with/without Au NPs of different size (19, 66, and 106 nm). The final concentrations of Au NPs and PpIX in all sets of measurement were 40 and 3.33 μM, respectively. Serum-free medium was used as control. After incubation for 4 h with the medium containing different reagents, the cells were carefully rinsed with Hank's buffered salt solution (HBSS) under a dark condition and then maintained in 100 μL of HBSS. The cells were irradiated with a broad-band light source using a 150 W halogen lamp (Dolan-Jenner Fiber-Lite MI-150) for 1 min. After irradiation, HBSS was removed and the well was replaced with complete cell culture medium and incubated for 24 h prior to cell viability assessment.

***In Vitro* Cell Viability Assessment.** The viability of cells after treatment was determined by the thiazolyl blue tetrazolium bromide (MTT, Sigma) assay. Briefly, the culture was incubated with MTT in cell culture medium (0.5 mg/mL) for 2 h. After discarding the nonreacted solution, 100 μL of dimethyl sulfoxide (DMSO, Sigma) was added to extract the formazan crystals. Absorbance of the extract was measured at 570 nm with BioTek microplate reader. The experiment was repeated at least three times.

Cellular Uptake of Au NPs. To determine the size-dependent uptake of Au NPs by breast cancer cells, Au NPs of different sizes were mixed with the cell culture medium at the same concentration of gold and added into cells with an identical cell density. After incubation for 4 h, free particles were removed by washing thoroughly with HBSS for at least three times. The cells were then trypsinized, centrifuged, and washed with HBSS. The collected cells were lysed with an alkaline buffer consisting of sodium dodecyl sulfate (SDS) and 1 N sodium hydroxide. The released Au NPs were quantified by the spectrometric assay after normalization. The normalization was done *via* the areas under the UV absorbance spectrum (400 to 800 nm); that is, the area was calculated in all of the groups and then subtracted with the untreated control group.

Measurement of Singlet Oxygen Species. To measure the cellular ROS formation after PDT treatment, singlet oxygen sensor green reagent (SOSG, Sigma), specifically for singlet oxygen species, was used according to manufacturer's protocol. In the presence of singlet oxygen species, SOSG emits a detectable green fluorescence. Briefly, a final SOSG concentration of 1.33 μM in HBSS was incubated with the cells, and the fluorescence intensity was measured using the microplate reader with the excitation wavelength at 485/20 nm and the emission wavelength at 528/20 nm.

Conflict of Interest: The authors declare no competing financial interest.

Acknowledgment. We gratefully acknowledge Mr. Yevgeniy Davletshin of Ryerson University, Canada, for providing a nanosphere model file through the COMSOL model exchange program. Y.Y. was supported by Innovation & Entrepreneurship Doctoral Fellowship from Stevens Institute of Technology. This research effort used microscope resources was partially funded by the National Science Foundation through NSF Grant DMR-0922522.

Supporting Information Available: The experimental results of control samples. This material is available free of charge *via* the Internet at http://pubs.acs.org.

REFERENCES AND NOTES

1. Foote, C. S. Photosensitized Oxygenations and the Role of Singlet Oxygen. *Acc. Chem. Res.* **1968**, *1*, 104–110.
2. Gius, D.; Spitz, D. Redox Signaling in Cancer Biology. *Antioxid. Redox Signaling* **2006**, *8*, 1249–1252.
3. Buttke, T. M.; Sandstrom, P. A. Oxidative Stress as a Mediator of Apoptosis. *Immunol. Today* **1994**, *15*, 7–10.
4. Palumbo, G. Photodynamic Therapy and Cancer: A Brief Sightseeing Tour. *Expert Opin. Drug Delivery* **2007**, *4*, 131–148.
5. Iani, V.; Moan, J.; Ma, L.-W. In *Measurements of Light Penetration into Human Tissues in Vivo*; Ehrenberg, B., Jori, G., Moan, J., Eds.; SPIE: Barcelona, Spain, 1996; pp 378−383.
6. Detty, M. R.; Gibson, S. L.; Wagner, S. J. Current Clinical and Preclinical Photosensitizers for Use in Photodynamic Therapy. *J. Med. Chem.* **2004**, *47*, 3897–3915.
7. Allison, R. R.; Downie, G. H.; Cuenca, R.; Hu, X.-H.; Childs, C. J. H.; Sibata, C. H. Photosensitizers in Clinical PDT. *Photodiagn. Photodyn. Ther.* **2004**, *1*, 27–42.
8. Castano, A. P.; Demidova, T. N.; Hamblin, M. R. Mechanisms in Photodynamic Therapy: Part One—Photosensitizers, Photochemistry and Cellular Localization. *Photodiagn. Photodyn. Ther.* **2004**, *1*, 279–293.
9. Moser, J. G. *Photodynamic Tumor Therapy: 2nd and 3rd Generation Photosensitizers*; Taylor & Francis: Boca Raton, FL, 1998.
10. Ballico, M.; Rapozzi, V.; Xodo, L. E.; Comuzzi, C. Metallation of Pentaphyrin with Lu(III) Dramatically Increases Reactive-Oxygen Species Production and Cell Phototoxicity. *Eur. J. Med. Chem.* **2011**, *46*, 712–720.
11. Wang, Y.; He, Q.-Y.; Che, C.-M.; Tsao, S. W.; Sun, R. W.-Y.; Chiu, J.-F. Modulation of Gold(III) Porphyrin 1a-Induced Apoptosis by Mitogen-Activated Protein Kinase Signaling Pathways. *Biochem. Pharmacol.* **2008**, *75*, 1282–1291.
12. Dougherty, T. J.; Gomer, C. J.; Henderson, B. W.; Jori, G.; Kessel, D.; Korbelik, M.; Moan, J.; Peng, Q. Photodynamic Therapy. *J. Natl. Cancer Inst.* **1998**, *90*, 889–905.
13. Peng, Q.; Warloe, T.; Berg, K.; Moan, J.; Kongshaug, M.; Giercksky, K. E.; Nesland, J. M. 5-Aminolevulinic Acid-Based Photodynamic Therapy: Clinical Research and Future Challenges. *Cancer* **1997**, *79*, 2282–2308.
14. Wang, I.; Bendsoe, N.; Klinteberg, C. A. f.; Enejder, A. M. K.; Andersson-Engels, S.; Svanberg, S.; Svanberg, K. Photodynamic Therapy *vs*. Cryosurgery of Basal Cell Carcinomas: Results of a Phase III Clinical Trial. *Br. J. Dermatol.* **2001**, *144*, 832–840.
15. Morton, C. A.; Whitehurst, C.; McColl, J. H.; Moore, J. V.; MacKie, R. M. Photodynamic Therapy for Large or Multiple Patches of Bowen Disease and Basal Cell Carcinoma. *Arch. Dermatol.* **2001**, *137*, 319–324.
16. Konan, Y. N.; Gurny, R.; Allémann, E. State of the Art in the Delivery of Photosensitizers for Photodynamic Therapy. *J. Photochem. Photobiol., B* **2002**, *66*, 89–106.
17. Lee, S. J.; Park, K.; Oh, Y.-K.; Kwon, S.-H.; Her, S.; Kim, I.-S.; Choi, K.; Lee, S. J.; Kim, H.; Lee, S. G.; Kim, K.; Kwon, I. C. Tumor Specificity and Therapeutic Efficacy of Photosensitizer-Encapsulated Glycol Chitosan-Based Nanoparticles in Tumor-Bearing Mice. *Biomaterials* **2009**, *30*, 2929–2939.
18. Zeisser-Labouèbe, M.; Delie, F.; Gurny, R.; Lange, N. Benefits of Nanoencapsulation for the Hypercin-Mediated Photodetection of Ovarian Micrometastases. *Eur. J. Pharm. Biopharm.* **2009**, *71*, 207–213.
19. Roy, I.; Ohulchanskyy, T. Y.; Pudavar, H. E.; Bergey, E. J.; Oseroff, A. R.; Morgan, J.; Dougherty, T. J.; Prasad, P. N. Ceramic-Based Nanoparticles Entrapping Water-Insoluble Photosensitizing Anticancer Drugs: A Novel Drug-Carrier System for Photodynamic Therapy. *J. Am. Chem. Soc.* **2003**, *125*, 7860–7865.
20. Yaghini, E.; Seifalian, A. M.; MacRobert, A. J. Quantum Dots and Their Potential Biomedical Applications in Photosensitization for Photodynamic Therapy. *Nanomedicine* **2009**, *4*, 353–363.
21. Wieder, M. E.; Hone, D. C.; Cook, M. J.; Handsley, M. M.; Gavrilovic, J.; Russell, D. A. Intracellular Photodynamic Therapy with Photosensitizer-Nanoparticle Conjugates: Cancer Therapy Using a 'Trojan Horse'. *Photochem. Photobiol. Sci.* **2006**, *5*, 727–734.
22. Olivo, M.; Bhuvaneswari, R.; Lucky, S. S.; Dendukuri, N.; Soo-Ping Thong, P. Targeted Therapy of Cancer Using Photodynamic Therapy in Combination with Multi-faceted Antitumor Modalities. *Pharmaceuticals* **2010**, *3*, 1507–1529.
23. Josefsen, L. B.; Aylott, J. W.; Beeby, A.; Warburton, P.; Boyle, J. P.; Peers, C.; Boyle, R. W. Porphyrin-Nanosensor Conjugates. New Tools for the Measurement of Intracellular Response to Reactive Oxygen Species. *Photochem. Photobiol. Sci.* **2010**, *9*, 801–811.
24. Vanderesse, R.; Frochot, C.; Barberi-Heyob, M.; Richeter, S.; Raehm, L.; Durand, J.-O. Nanoparticles for Photodynamic Therapy Applications. In *Intracellular Delivery*; Springer: Berlin, 2011; Vol. 5, pp 511−565.
25. Shukla, R.; Bansal, V.; Chaudhary, M.; Basu, A.; Bhonde, R. R.; Sastry, M. Biocompatibility of Gold Nanoparticles and Their Endocytotic Fate Inside the Cellular Compartment: A Microscopic Overview. *Langmuir* **2005**, *21*, 10644–10654.
26. Wenfu, Y.; Suree, B.; Zhengwei, P.; Shannon, M. M.; Steven, H. O.; Sheng, D. Ultrastable Gold Nanocatalyst Supported by Nanosized Non-oxide Substrate. *Angew. Chem., Int. Ed.* **2006**, *45*, 3614–3618.
27. Jain, P. K.; Lee, K. S.; El-Sayed, I. H.; El-Sayed, M. A. Calculated Absorption and Scattering Properties of Gold Nanoparticles of Different Size, Shape, and Composition: Applications in Biological Imaging and Biomedicine. *J. Phys. Chem. B* **2006**, *110*, 7238–7248.
28. Njoki, P. N.; Lim, I. I. S.; Mott, D.; Park, H.-Y.; Khan, B.; Mishra, S.; Sujakumar, R.; Luo, J.; Zhong, C.-J. Size Correlation of Optical and Spectroscopic Properties for Gold Nanoparticles. *J. Phys. Chem. C* **2007**, *111*, 14664–14669.
29. El-Brolossy, T. A.; Abdallah, T.; Mohamed, M. B.; Abdallah, S.; Easawi, K.; Negm, S.; Talaat, H. Shape and Size Dependence of the Surface Plasmon Resonance of Gold Nanoparticles Studied by Photoacoustic Technique. *Eur. Phys. J* **2008**, *153*, 361–364.
30. Khaing Oo, M. K.; Yang, X.; Du, H.; Wang, H. 5-Aminolevulinic Acid-Conjugated Gold Nanoparticles for Photodynamic Therapy of Cancer. *Nanomedicine* **2008**, *3*, 777–786.
31. Guo, H.; Ruan, F.; Lu, L.; Hu, J.; Pan, J.; Yang, Z.; Ren, B. Correlating the Shape, Surface Plasmon Resonance, and Surface-Enhanced Raman Scattering of Gold Nanorods. *J. Phys. Chem. C* **2009**, *113*, 10459–10464.

32. Turkevich, J.; Stevenson, P. C.; Hillier, J. A Study of the Nucleation and Growth Processes in the Synthesis of Colloidal Gold. *Discuss. Faraday Soc.* **1951**, *11*, 55–75.
33. Frens, G. Controlled Nucleation for the Regulation of the Particle Size in Monodisperse Gold Suspensions. *Nature* **1973**, *241*, 20–22.
34. Ghosh, S. K.; Pal, T. Interparticle Coupling Effect on the Surface Plasmon Resonance of Gold Nanoparticles: From Theory to Applications. *Chem. Rev.* **2007**, *107*, 4797–4862.
35. Ding, H.; Sumer, B. D.; Kessinger, C. W.; Dong, Y.; Huang, G.; Boothman, D. A.; Gao, J. Nanoscopic Micelle Delivery Improves the Photophysical Properties and Efficacy of Photodynamic Therapy of Protoporphyrin IX. *J. Controlled Release* **2011**, *151*, 271–277.
36. Samia, A. C. S.; Chen, X.; Burda, C. Semiconductor Quantum Dots for Photodynamic Therapy. *J. Am. Chem. Soc.* **2003**, *125*, 15736–15737.
37. Soh, N. Recent Advances in Fluorescent Probes for the Detection of Reactive Oxygen Species. *Anal. Bioanal. Chem.* **2006**, *386*, 532–543.
38. Crow, J. P. Dichlorodihydrofluorescein and Dihydrorhodamine 123 Are Sensitive Indicators of Peroxynitrite *in Vitro*: Implications for Intracellular Measurement of Reactive Nitrogen and Oxygen Species. *Nitric Oxide* **1997**, *1*, 145–157.
39. Johnson, P. B.; Christy, R. W. Optical Constants of the Noble Metals. *Phys. Rev. B* **1972**, *6*, 4370.
40. Kerker, M.; Wang, D.-S.; Chew, H. Surface Enhanced Raman Scattering (SERS) by Molecules Adsorbed at Spherical Particles. *Appl. Opt.* **1980**, *19*, 4159–4174.
41. Le Ru, E. C.; Etchegoin, P. G.; Meyer, M. Enhancement Factor Distribution Around a Single Surface-Enhanced Raman Scattering Hot Spot and Its Relation to Single Molecule Detection. *J. Chem. Phys.* **2006**, *125*, 204701-13.
42. Franzen, S. Intrinsic Limitations on the $|E|^4$ Dependence of the Enhancement Factor for Surface-Enhanced Raman Scattering. *J. Phys. Chem. C* **2009**, *113*, 5912–5919.
43. Chowdhury, J.; Pal, P.; Ghosh, M.; Misra, T. N. Surface-Enhanced Raman Scattering of Rhodamine 123 in Silver Hydrosols and in Langmuir−Blodgett Films on Silver Islands. *J. Colloid Interface Sci.* **2001**, *235*, 317–324.
44. Khaing Oo, M. K.; Chang, C.-F.; Sun, Y.; Fan, X. Rapid, Sensitive DNT Vapor Detection with UV-Assisted Photochemically Synthesized Gold Nanoparticle SERS Substrates. *Analyst* **2011**, *136*, 2811–2817.
45. Ito, S.; Miyoshi, N.; Degraff, W. G.; Nagashima, K.; Kirschenbaum, L. J.; Riesz, P. Enhancement of 5-Aminolevulinic Acid-Induced Oxidative Stress on Two Cancer Cell Lines by Gold Nanoparticles. *Free Radical Res.* **2009**, *43*, 1214–1224.
46. Suttorp, N.; Toepfer, W.; Roka, L. Antioxidant Defense Mechanisms of Endothelial Cells: Glutathione Redox Cycle *versus* Catalase. *Am. J. Physiol. Cell Physiol.* **1986**, *251*, C671–C680.
47. Pelicano, H.; Carney, D.; Huang, P. ROS Stress in Cancer Cells and Therapeutic Implications. *Drug Resist. Updates* **2004**, *7*, 97–110.
48. Chithrani, B. D.; Ghazani, A. A.; Chan, W. C. W. Determining the Size and Shape Dependence of Gold Nanoparticle Uptake into Mammalian Cells. *Nano Lett.* **2006**, *6*, 662–668.
49. Korbelik, M.; Sun, J.; Cecic, I. Photodynamic Therapy−Induced Cell Surface Expression and Release of Heat Shock Proteins: Relevance for Tumor Response. *Cancer Res.* **2005**, *65*, 1018–1026.
50. Castano, A. P.; Demidova, T. N.; Hamblin, M. R. Mechanisms in Photodynamic Therapy: Part Two—Cellular Signaling, Cell Metabolism and Modes of Cell Death. *Photodiagn. Photodyn. Ther.* **2005**, *2*, 1–23.